energies

MDPI

Article

Biomimetic Design for Enhanced Thermal Performance of Vapor Chambers

Jingyu Shen [1,2] and Ce Guo [1,2,*]

[1] College of Mechanical and Electrical Engineering, Nanjing University of Aeronautics and Astronautics, Nanjing 210016, China; shenjy_2020@163.com
[2] Institute of Bio-Inspired Structure and Surface Engineering, Nanjing University of Aeronautics and Astronautics, Nanjing 210016, China
* Correspondence: guozc@nuaa.edu.cn

Abstract: Vapor chambers (VCs) are efficient heat spreaders that rely on wicks to realize the circulation of a phase-changing working liquid and can be used to address heat dissipation problems in electronic devices, aerospace, and satellite equipment. In this study, we propose a novel vapor chamber with biomimetic wick structures and composite lattice supports to enhance the thermal management and load-bearing performance of vapor chambers. The experiments and COMSOL multiphysics 6.1 simulation results indicate that the biomimetic design can improve the startup performance, thermal management, and load-bearing performance of the VC. Compared to conventional VCs, at a filling ratio of 20% the biomimetic VC reduces the time to reach a steady state by 11.7% and improves the uniformity of temperature by 7.74%. This study provides a novel design concept for VCs and verifies the operating performance of vapor in high heat flux density cases, providing a reference for the innovative design and enhanced heat transfer of phase change-based thermal management equipment.

Keywords: vapor chamber; thermal performance; multiphysics simulation; biomimetic design

check for updates

Academic Editor: Artur Blaszczuk

Received: 2 February 2025
Revised: 19 February 2025
Accepted: 28 February 2025
Published: 4 March 2025

Citation: Shen, J.; Guo, C. Biomimetic Design for Enhanced Thermal Performance of Vapor Chambers. *Energies* **2025**, *18*, 1250. https://doi.org/10.3390/en18051250

Copyright: © 2025 by the authors. Licensee MDPI, Basel, Switzerland. This article is an open access article distributed under the terms and conditions of the Creative Commons Attribution (CC BY) license (https://creativecommons.org/licenses/by/4.0/).

1. Introduction

A vapor chamber (VC), which is also known as a flat heat pipe, can effectively improve the temperature nonuniformity caused by heat concentration through two-phase cycles. It is a guided thermal protection structure and has the advantages of high thermal conductivity, good isothermal performance, strong stability, strong heat transfer capacity, reliable operation, and a high working temperature. A VC is a practical means to eliminate hot spots under high-temperature nonuniformity and is widely used in high-speed aircraft [1], nuclear reactor power [2], electric vehicle thermal management systems [3], batteries [4], solar energy collection [5], waste heat recovery, electronic equipment heat dissipation, and other fields.

As an efficient heat transfer device, a VC relies mainly on wicks to achieve phase change circulation of the internal working fluid to evenly distribute heat and eliminate hot spots. When locally heated, the liquid working fluid in the evaporator inside the VC absorbs heat and turns into vapor. The vapor moves from the evaporator to the condenser under the drive of pressure difference. When it reaches the condenser, the vapor condenses into a liquid and releases heat. The working fluid in the condenser returns to the evaporator under the action of wicks. During the continuous repetition of the above process, the working fluid continues to circulate, transporting heat from the evaporator to the condenser and thus balancing the temperatures of different parts.

Currently, with improvements in equipment performance, the requirements for VC thermal management, its lightweight properties, and other functions have increased. Therefore, optimizing the design of VCs is a key issue that needs to be addressed. The traditional VC is mainly composed of a shell, wicks, and working fluid. The shell and working fluid are mainly determined by the actual application conditions. In the case where the main structure is known, the improvement in heat pipe performance depends on the wicks used to promote two-phase heat conduction [6]. Therefore, the key to improving VC performance lies in designing new wicks. At present, wicks are mainly divided into sintered powder, wire mesh [7–9], microgrooves [10], and composite wicks formed by combining the above structures [11,12].

Recently, innovative designs and developments have emerged for wicks [13]. For example, Li [14] proposed a multi-scale microgrooved wick structure fabricated with sintered copper powder, which showed a greater capillary pumping amount and wicking velocity in the capillary rise process compared to the plain sintered powder wicks (PCPWs) and sintered powder wicks covered by nanograss (NGPWs). Ryu [15] proposed dual-height superhydrophilic micropost evaporator wicks with improved heat transfer performance for thermal management applications, which enhances the heat transfer coefficient by up to 300%, and decreases the sensitivity of heat transfer and capillary performance to liquid-filled charges by over 60% compared with previous single-height micropost wicks. Peng [16,17] used micro fin-pin arrays and leaf-vein-like fractal architecture channels to form porous media as liquid wicks. The results showed that the wick greatly affected the temperature and pressure drop, improving the heat and mass transfer performance of the overall structure over that of the conventional structure. Liu [18] proposed a novel method for optimizing the layout of the grooved evaporator wick structure of a vapor chamber heat spreader, which was inspired by natural branches and based on growth simulation, to obtain a topological structure with dichotomous, hierarchical, and branching characteristics, which improved the capillary pressure and made the temperature gradient more homogeneous. This method enables the vapor chamber heat spreader to have better heat dissipation performance. Cui [19] used a thermal oxidation method to treat ultrathin heat pipe wire mesh wicks so that the water droplets were changed from being pinned on the wick surface to being completely immersed in the wick. The study revealed that the proposed ultrathin heat pipe is a reliable candidate for the thermal management of electronic devices with high heat transfer rates. Koukoravas [20] proposed a design that replaced the condenser wick and wicking posts with a wettability-patterned plate and measured the dependence of the vapor chambers on orientation through experiments. The results showed that incorporating wettability patterns into vapor chamber heat spreaders has broad potential.

Support columns can be set up in a VC on the basis of the requirements of the application scenario to ensure the strength and stability of the overall structure [11,21]. However, common support columns mainly use solid structures [22,23], causing a sudden increase in VC mass, which is not desirable in fields such as aerospace and portable devices that require highly lightweight materials. Lattice structures, as lightweight and high-strength support structures, are excellent alternatives to solid structures and, as porous structures, have more advantages than solid supports in terms of vapor flow and liquid transport inside the vapor chamber. Therefore, referring to the lattice bearing structure for VCs has great potential. Overall, as an efficient heat dissipation structure, current VC designs have considerable optimization potential on the basis of surface modifications, biomimetic designs, and other applications.

However, current research on vapor chambers mainly focuses on optimizing individual components such as wick structures and support columns without systematically optimizing the overall structure. This local optimization strategy only addresses a single performance index, resulting in improvements confined to the specific performance, which thus demonstrates limited effectiveness in comprehensively elevating the holistic performance of the vapor chamber, particularly regarding critical parameters like startup performance, temperature uniformity, and load-bearing capacity. Therefore, we propose an integrated biomimetic optimization strategy based on our previous study. On the basis of bionic similarity principles, and inspired by the optimized features of biological structures, various components of the vapor chamber are optimized multi-dimensionally to enhance the comprehensive performance of the vapor chamber.

In this study, biomimetic designs were created for wicks of a vapor chamber. Inspired by the superhydrophobic and superhydrophilic properties of lotus leaves and mosses in nature, we designed wicks with a superhydrophilic evaporation section and a superhydrophobic condensation section to increase the transport efficiency of the working fluid in phase-changing circulation. In addition, biomimetic grooves were machined on wicks inspired by the capillary transport characteristics of leaf veins to help the liquid working fluid flow back to the heat source and thus shorten the period of phase-changing circulation. From the perspective of being both lightweight and high strength, a lattice support structure was designed and prepared through 3D printing additive manufacturing. The lattice support was wrapped with a vertical wick, which was the so-called composite support column, to increase the flow path of the liquid working fluid. In terms of the simulation analysis method, the COMSOL multiphysics 6.1 simulation method was adopted to analyze the temperature distribution of the saturated vapor chamber, and the contribution of each component to heat transfer was obtained by calculating the heat transfer rate. The important role of lattices in bearing loads was analyzed by applying pressure on the upper surface of the VC. Finally, on the basis of the above optimized designs, a novel vapor chamber was prepared, and a thermal testing platform was built. The thermal management function of the biomimetic wicks was analyzed experimentally. The results indicate that the biomimetic design improved the VC by shortening the steady-state time and enhancing the heat dissipation performance.

2. Materials and Methods

2.1. Prototype of the Vapor Chamber with Biomimetic Wicks

In this work, the thermal performance of a VC was enhanced by the biomimetic designs of the condenser and the evaporator wicks (Figure 1a). Inspired by the hydrophobicity of lotus leaf surfaces, which allows quick movement of water droplets, and the hydrophilicity of moss, which keeps it moist, superhydrophobic and superhydrophilic surfaces are implemented onto the condenser and the evaporator wicks, respectively. As the superhydrophobic surface can promote the formation of dropwise condensation, droplets quickly form and fall off the condensation surface, continuously exposing the surface to the vapor and maintaining efficient heat transfer. In contrast, during the evaporation process of the working fluid, the superhydrophilic property of the evaporator wick surface makes it easier for the working liquid to spread and infiltrate the surface, increasing the contact area between the working fluid and the evaporation surface, which helps form a uniform liquid film and promotes the generation and detachment of bubbles during nucleate boiling, thereby improving the evaporation efficiency and thermal performance.

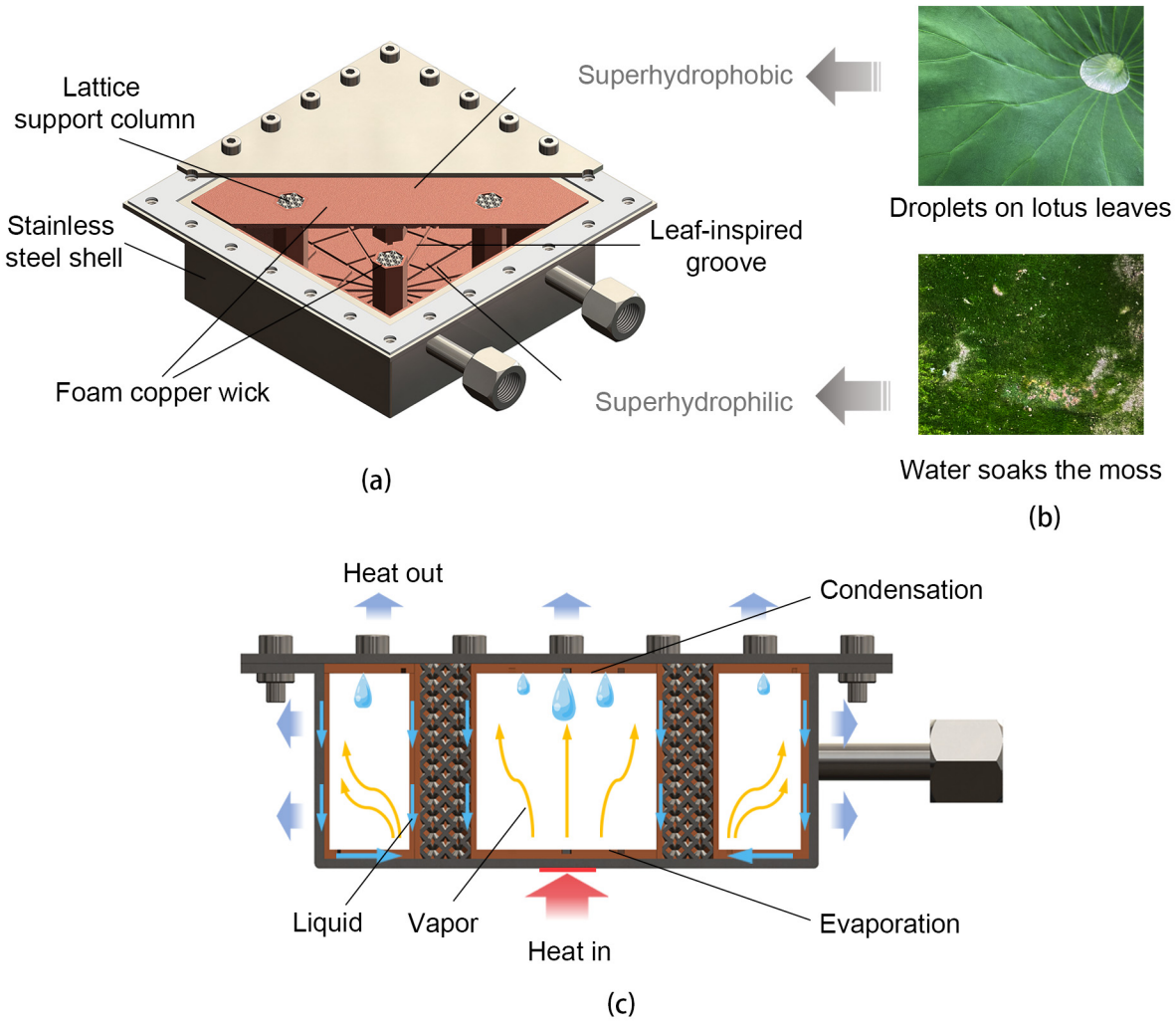


Figure 1. (**a**) Schematic of the biomimetic VC structure. (**b**) Inspirations for the biomimetic VC. (**c**) Schematic illustration of the VC operation principle.

In addition to the surface modification treatments, biomimetic grooves were also introduced on the condenser and the evaporator wicks, the design of which was based on our previous work [24]. Bioinspired by the leaf vein structures with efficient capillary transport in plants, the grooves were designed on the basis of typical leaf vein features such as wedge-shaped structures and asymmetric branches. Compared with those of conventional porous copper foam, the capillary force and permeability of a wick with grooves are more balanced. This composite wick structure can effectively separate the gas–liquid flow path and enhance capillary transport. As Figure 1c shows, the design of the grooves allows the droplets to gather above the heat source, thereby shortening the time for the liquid to reflux to the heat source.

Considering the lightweight and load-bearing requirements of aircraft, satellites, and other devices, a composite column that comprises a honeycomb-shaped 3D-printed lattice structure and a porous copper foam (which is wrapped on the lattice) is proposed. The lattice structure was designed to bear loads within the VC, and the vertical wick was conducive to the upward and downward transport of the working fluid.

Figure 2 shows a biomimetic designed vapor chamber which comprises a metal shell, four lattice support columns, and wick structures. The shell, assembled through fasteners and sealed with a silicone gasket, was manufactured via a series of processes, including laser cutting, bending, welding, and was welded with two G1/4 connection joints. Copper foam was used to fabricate the wick structures, which were full of the internal surfaces of the shell.

The upper superhydrophobic wick was the condenser, and the lower superhydrophilic wick was the evaporator, with biomimetic grooves milled on both surfaces. The tight fit between the wicks and the shell was enabled by the accurate dimensions and soldering process. The 3D-printed lattices of the composite support columns were made of 316 stainless steels, and the working fluid was deionized water. Table 1 summarizes the specifications of the VC sample.

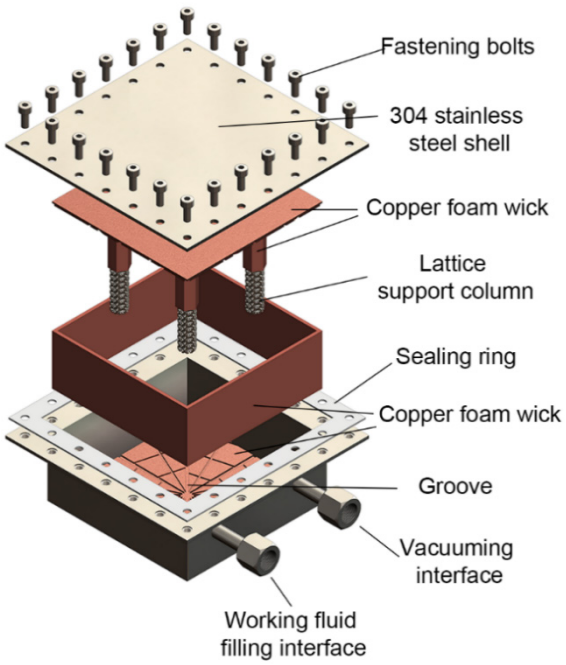


Figure 2. Schematic of the structure of the novel vapor chamber.

Table 1. Geometric parameters of the vapor chamber.

Geometrical Parameter	Value
Area of bottom surface	100 mm × 100 mm
Size of top surface	120 mm × 120 mm
Vapor chamber height	40 mm
Shell thickness	1.5 mm
Wick thickness	2 mm
Self-clinching nuts	M4 SUS304
Bolts	M4 × 10 SUS304
Sealing gasket	2 mm silicone gasket

2.2. Vapor Chamber Fabrication

2.2.1. Leaf Vein Inspired Grooves

In this investigation, copper foam with 97% porosity served as the base material for the wicks, and Table 2 lists the complete details of the copper foam. Copper foam has the following advantages. First, the copper foam is a porous medium, where the larger pores are instrumental in vapor escape, and the smaller pores facilitate the liquid capillary transmission. Thus, the pores of copper foam are conducive to orderly movement and circulation between vapor and liquid. Second, grooves can be fabricated on copper foam more easily than mesh wicks and sintered copper wicks.

Table 2. Parameters of the copper foam wick.

Parameter	Value
Porosity	97%
Surface density	Approximate 500–600 g/m^2
Pore size	100–200 μm

The capillary transport grooves were designed based on the wedge-shaped and asymmetric branch features of the leaf vein structure, which were summarized in our previous study [24]. The efficient transmission mechanism of these features was validated through theoretical derivation and numerical analysis. In this study, the grooves with these leaf vein inspired features were applied to the VC system. High-speed CNC (computer numerical control) milling technology was used to process the grooves at a depth of 1 mm on the surface of the wick to avoid material blockage, which may be caused by laser processing, mold imprinting, and other methods [25]. In detail, the precise microchannels on the copper foam substrate were processed in a vertical machining center (Model TL-650D, Kunshan Taizhicheng Precision Machinery Co., Ltd., Kunshan, China). To ensure the fixation of the workpiece during the machining process, a self-adhesive polymer film was applied to the non-machined surface, with the opposing film surface anchored to a vacuum chuck of the machining center. Then, three processes were employed to machine the channels, with drills of three different diameters (∅2 mm, ∅1 mm, and ∅0.8 mm) used, respectively. Finally, the polymer film of the copper foam substrate was removed after the completion of the whole machining process. Figure 3 shows the processed capillary wick.

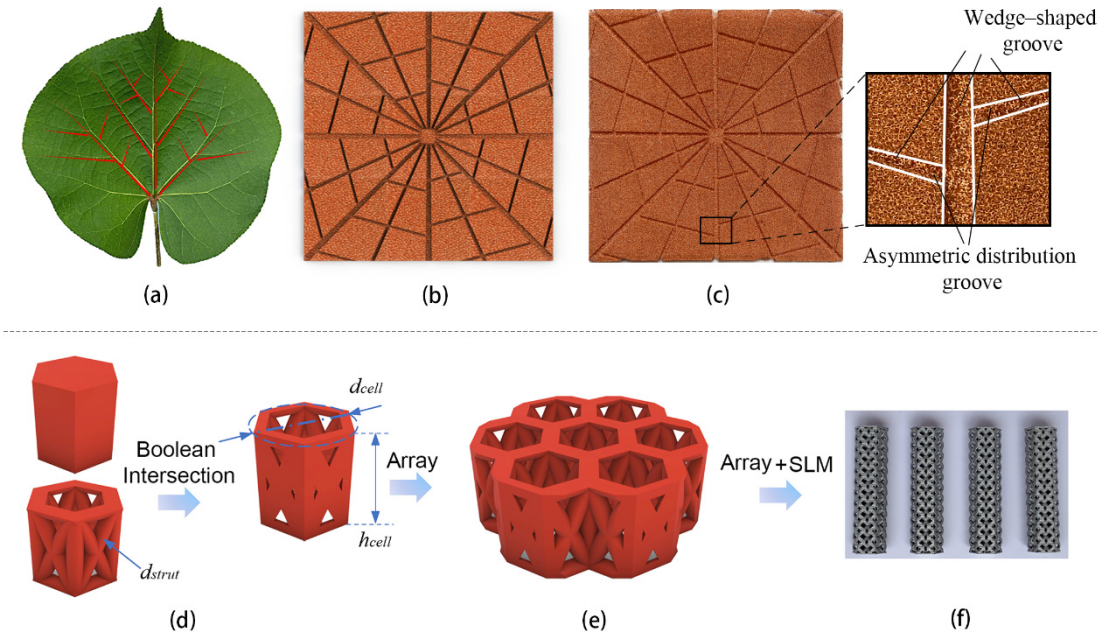


Figure 3. (**a**) Schematic of leaf vein capillary channels. (**b**) Schematic of biomimetic channels. (**c**) Precision milling grooves on the copper foam and their detailed characteristics. (**d**) Unit cell structure of the support lattice. (**e**) Support lattice formed by a hexagonal array of unit cells, and (**f**) support lattices processed by SLM.

2.2.2. Surface Modification Treatment

A pretreatment process was incorporated to obtain clean copper foam before surface modification was performed for the condenser and evaporator wicks. The copper foam was first immersed in a HCl solution to remove the surface residue, then placed in an

ultrasonic cleaning machine for 30 min to thoroughly remove surface and internal residues, and finally, it was rinsed with deionized water to remove the residual HCl.

The fabrication process of the superhydrophobic condenser wick is as follows [26]. The copper foam sample was first soaked in 0.03 mol/L ammonia solution for 48 h and then rinsed with deionized water. After being heated in a 180 °C oven for 2 h, the sample was placed in a 0.5 wt% hexane solution with 1H,1H,2H,2H-perfluorodecyltriethoxysilane for 1 h. Finally, the copper foam wick was dried in a 110 °C oven for 1 h to promote the reaction between the 1H,1H,2H,2H-perfluorodecyltriethoxysilane and the copper foam surface, thus increasing the stability and firmness of the hydrophobic coating and helping to further solidify and stabilize the surface modification layer, making it more uniform and firmer.

Chemical treatment was performed on the evaporator wick surface to form a superhydrophilic coating of CuO. First, a mixed solution of 0.065 mol/L $K_2S_2O_8$ and 2.5 mol/L KOH was prepared, which was then placed in a water bath at a constant temperature of 70 °C to achieve the same temperature. Second, the copper foam sample was immersed completely in the mixed solution for 30 min and rinsed with deionized water. The washed sample was finally dried in a 180 °C vacuum drying oven for 30 min [4,27]. After the reaction, the surfaces of the copper foam became black, and the original metallic luster disappeared. The chemical equation for this reaction is as follows:

$$Cu + 2KOH + K_2S_2O_8 \rightarrow Cu(OH)_2 + 2K_2SO_4$$

$$Cu(OH)_2 \rightarrow CuO + H_2O$$

2.2.3. Lightweight Honeycomb Lattice Column

To ensure load-bearing performance, support columns are usually set in the VC, and common columns include sintered and solid columns [4,28]. The reasonable design of the support structure can also help with the thermal management of the VC. With the popularization of 3D printing technology, lightweight lattice structures are gradually emerging in the context of load-bearing ability.

Owing to the exceptional stability and array properties of the honeycomb structure, and the excellent lightweight characteristics of the lattice structure, we designed a lattice structure with a honeycomb for the support ability of the vapor chamber (Figure 3). The design process is as follows: first, a unit cell structure based on the honeycomb-shaped junction center form is designed; then, through a Boolean intersection operation, it becomes a regular unit cell that is easy to array. This type of unit cell forms a lattice bearing structure for the interior of the vapor chamber through arrays.

Owing to the flexibility of additive manufacturing technology, this study used 3D printing equipment (Model HBD-150, Shanghai Hanbang United Airlines Laser Technology Co., Ltd., Shanghai, China) with selective laser melting technology to prepare samples, and Table 3 lists the equipment model and process parameters. During the printing process, the molten metal powder gradually accumulates on the substrate to form a lattice structure. To ensure the support function of the lattice structure and its assembly with the shell, thin planes are set at the upper and lower ends of the lattice structure. After printing, the lattice structure is removed from the substrate by wire cutting and immersed in ethanol solution for ultrasonic cleaning to remove residual dirt during the preparation process. Figure 3f shows the prepared sample. This structure not only has the load-bearing characteristic of the traditional hexagonal honeycomb structure but also has the advantage of a lightweight lattice structure. Table 4 shows the specific parameters of the lattice.

Table 3. Technical parameters of the 3D printing equipment.

Forming Size	φ159 mm × 100 mm
Laser power	200 W, 200 W × 2
Layer thickness	10–40 μm
Scanning track width	40–80 μm
Scanning speed	<10,000 mm/s
Typical accuracy	0.05–0.1 mm

Table 4. Lattice parameters.

Lattice Porosity	Lattice Unit Cell Height (h_{cell})	Array Units
60%	3.5 mm	6 × 12

2.3. Experimental Setup

To analyze the influence of our biomimetic design on the startup characteristics and thermal performance of the vapor chamber, we construct a traditional VC for comparative experiments. In the traditional VC, there is no support column, and the wick is fabricated by the common copper foam without surface modification treatments or milled grooves.

An experimental testing system (Figure 4) is designed to achieve a high vacuum degree inside the vapor chamber, and then experiments on thermal performance can be carried out. The pressure transmitter and T-shaped tee are connected to the two welded pipe joints on the shell through threaded connections (with gaskets included for sealing). The T-shaped tee is connected to the vacuum pump and the working fluid injector, and both branches are equipped with vacuum ball valves. The pressure transmitter collects the pressure data inside the vapor chamber at a frequency of 60 times per second and transmits it to the computer via RS—485. Before each experiment, the internal pressure of the vapor chamber was evacuated to the vacuum state.

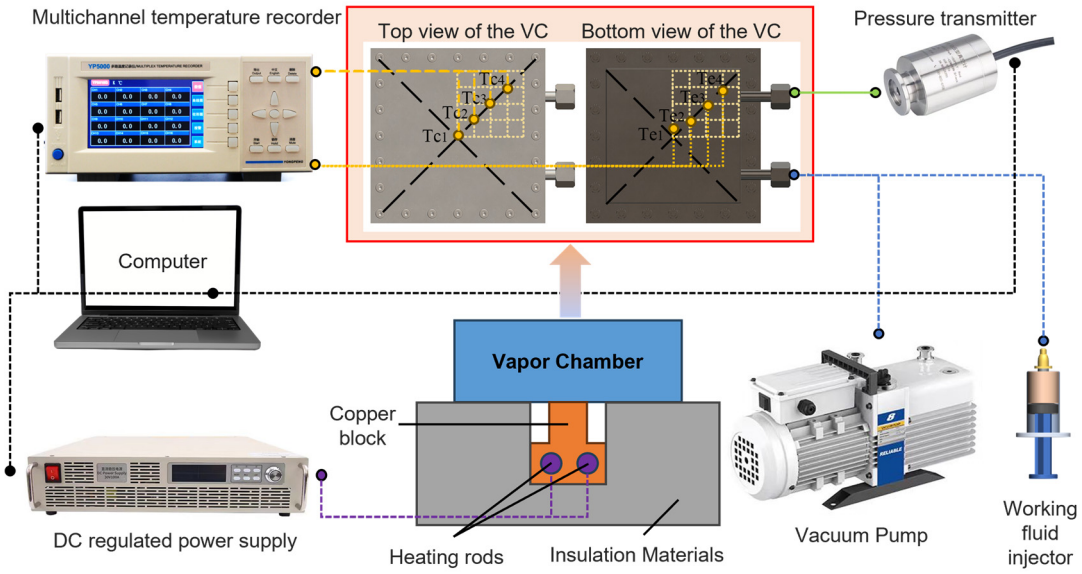


Figure 4. Schematic of the experimental setup.

2.3.1. Experimental Setup for the Thermal Performance of the VC

As Figure 4 shows, the VC is placed on the insulated boards, which have good insulation properties to prevent heat loss caused by heat transfer through the workbench. A copper block with two heating rods inserted into it was designed and processed, and the thermal power supplied to the heating rods can be set by using a DC regulated power

supply (Shanghai Aoshituo Electric Co., Ltd., Shanghai, China) with a constant power mode. The DC power supply was also connected to the computer via RS—485 to monitor the power value. A multichannel temperature recorder (Model YP5016G, Shenzhen Yongpeng Instrument Co., Ltd., Shenzhen, China) was used to obtain the surface temperature of the VC. The thermocouples were attached to the collection point with insulation tape. Except for the surface where the heat source was located, all other parts of the VC were exposed to the air, and the above surfaces exchange heat through convection and thermal radiation.

To comprehensively consider the influence of the liquid filling ratio on the results of the biomimetic design, this study uses three types of liquid filling ratios for analysis, and the formula for the liquid filling ratio is as follows [29,30]:

$$\varphi = \frac{V_l}{V_c} \tag{1}$$

where V_l is the volume of liquid working fluid and V_c is the volume of pores in the VC. We compare the thermal management performance of the biomimetic designed VC with a traditional VC through experiments.

2.3.2. Data Processing and Uncertainty Analysis

In this study, isothermal performance [31,32] and thermal resistance R_{th} are used to evaluate the thermal performance of the vapor chamber. The temperature uniformity coefficient (J) is an indicator used to evaluate the uniformity of the temperature distribution in a thermal system and reflects the extent of the temperature difference between the evaporator and condenser [6], and J can be calculated by the following equation:

$$J = 1 - \frac{T_{evap} - T_{cond}}{T_{evap}} \tag{2}$$

$$\begin{cases} T_{evap} = \sum_{i=1}^{4} T_{ei} \\ T_{cond} = \sum_{i=1}^{4} T_{ci} \end{cases} \tag{3}$$

where T_{evap} and T_{cond} are the average temperatures of the evaporation surface and the condensation surface, respectively, and can be calculated by the collection points shown in Figure 4 via Equation (3). Thus, the temperature uniformity coefficient J of the VC is obtained to evaluate its thermal management performance. The closer J is to 1, the smaller the temperature difference between the evaporation and condensation sections of the VC and the more uniform the temperature distribution. In contrast, the closer J is to 0, the greater the temperature difference and the more uneven the temperature distribution of the VC system.

The thermal resistance of a vapor chamber is a critical parameter for evaluating its thermal performance, defined as the ratio of the temperature difference (ΔT) generated across the vapor chamber to the input heat power (Q). R_{th} is formulated as follows:

$$R_{th} = \frac{\Delta T}{Q} = \frac{T_{cond} - T_{evap}}{Q} \tag{4}$$

The uncertainty of the experimental system was caused mainly by the heating source and thermocouples of the temperature recorder. The measurement error of the heating source was 2%, and the measurement accuracy of the temperature controller of the heating block was 1 °C, while the thermocouples were calibrated with a measurement accuracy of

0.6 °C. The relative measurement error of the thermal resistance can be calculated via the equation proposed by Kline and McClintock [25,33], which is as follows:

$$E(y) = \sqrt{\sum_{i=1}^{N} \left(\frac{\partial y}{\partial x_i} \cdot E(x_i) \right)^2} \tag{5}$$

where y is a given function of the independent variable x_i, $E(y)$ is the measurement error, and $E(x_i)$ is the maximum measurement error of the independent variable x_i. According to Equation (5), the maximum relative measurement uncertainty of the thermal resistance was 5.7%.

2.4. Multiphysics Simulation Analysis

The vapor chamber transfers heat in an orderly manner through evaporation, mass transfer, and condensation of the working fluid, and the two-phase heat and mass transfer inside it is a complex multiphysics coupling process. Because phase change cycles cannot be observed inside the vapor chamber, numerical simulation can better analyze the heat transfer performance of the vapor chamber. This method can be used to evaluate the engineering applicability of the structural design of a vapor chamber and is an essential part of its structural design.

2.4.1. Geometric Model and Boundary Conditions

The simulation analysis in this study is conducted using COMSOL multiphysics 6.1 software. Specifically, the "Laminar Flow Interface" and "Brinkman Equations Interface" from the CFD Module, as well as the "Heat Transfer Interface" from the Heat Transfer Module, are employed. In addition, the following assumptions are applied to simplify the numerical analysis:

(1) The vapor chamber is in a steady-state condition.
(2) The vapor is incompressible and the flow is laminar.
(3) The wick is a saturated, homogeneous porous medium, with fluid flow described by the Brinkman equation.

For the vapor region, the conservations of mass, momentum, and energy are considered. The corresponding equations include the continuity equation, Navier–Stokes equation, and energy equation, as can be seen in the following:

$$\begin{cases} \nabla \cdot \vec{u} = 0 \\ \rho_v \left(\vec{u} \cdot \nabla \right) \vec{u} = -\nabla p + \mu \nabla^2 \vec{u} + \vec{F} \\ \rho_v c_v \left(\vec{u} \cdot \nabla \right) T = k_v \nabla^2 T + Q \end{cases} \tag{6}$$

where $\vec{u}$ is the velocity, ρ_v is the density of the vapor, p is the pressure, μ is the dynamic viscosity, $\vec{F}$ is the external force term, c_v is the specific heat capacity of the vapor, k_v is the thermal conductivity of the vapor, T is the temperature, and Q is the heat source term.

For the wick, which is a porous material, the porosity is set to 97% according to the parameters of the copper foam wick used in the experiment. The solid phase of the wick material is copper, and the fluid phase within the pores is water. For the flow of the liquid working fluid in the wick's porous medium, the Brinkman equation is used for analysis. The Brinkman equation is a modified form of the Navier–Stokes equation that accounts for

fluid flow in porous media by incorporating a Darcy resistance term ($\frac{\mu}{K}\vec{u}$). Therefore, the governing equation for the fluid phase within the wick domain is as follows:

$$\begin{cases} \nabla\vec{u} = 0 \\ \rho_l\left(\vec{u}\cdot\nabla\right)\vec{u} = -\nabla p + \mu\nabla^2\vec{u} - \frac{\mu}{K}\vec{u} + \vec{F} \\ \rho_l c_l\left(\vec{u}\cdot\nabla\right)T = k_l\nabla^2 T + Q \end{cases} \tag{7}$$

where K is the permeability, ρ_l, c_l, and k_l are the density, specific heat capacity, and thermal conductivity of the liquid working fluid, respectively.

For the solid phase (copper) of the wick, the governing equation is as follows:

$$\rho_s c_s \nabla^2 T = 0 \tag{8}$$

where ρ_s and c_s are the density and specific heat capacity of the solid, respectively.

For the lattice support columns, which are involved in solid heat transfer, the governing equation is also as follows:

$$\rho_s c_s \nabla^2 T = 0 \tag{9}$$

For the shell region, the governing equation is as follows:

$$\nabla\cdot(k_s\nabla T) + q_{conv} + q_{rad} = 0 \tag{10}$$

where k_s is the thermal conductivity of the solid, q_{conv} is the convective heat flux, and q_{rad} is the radiative heat flux.

Regarding the boundary conditions, as shown in Figure 5, the heat source has dimensions of 10 mm × 10 mm and a heat input of q_{in}. The surface where the heat source is located is thermally insulated, while the remaining surfaces of the shell are heat dissipation surfaces, and heat transfer between the shell and the surrounding environment is through convection and radiation. Table 5 shows the specific parameters.

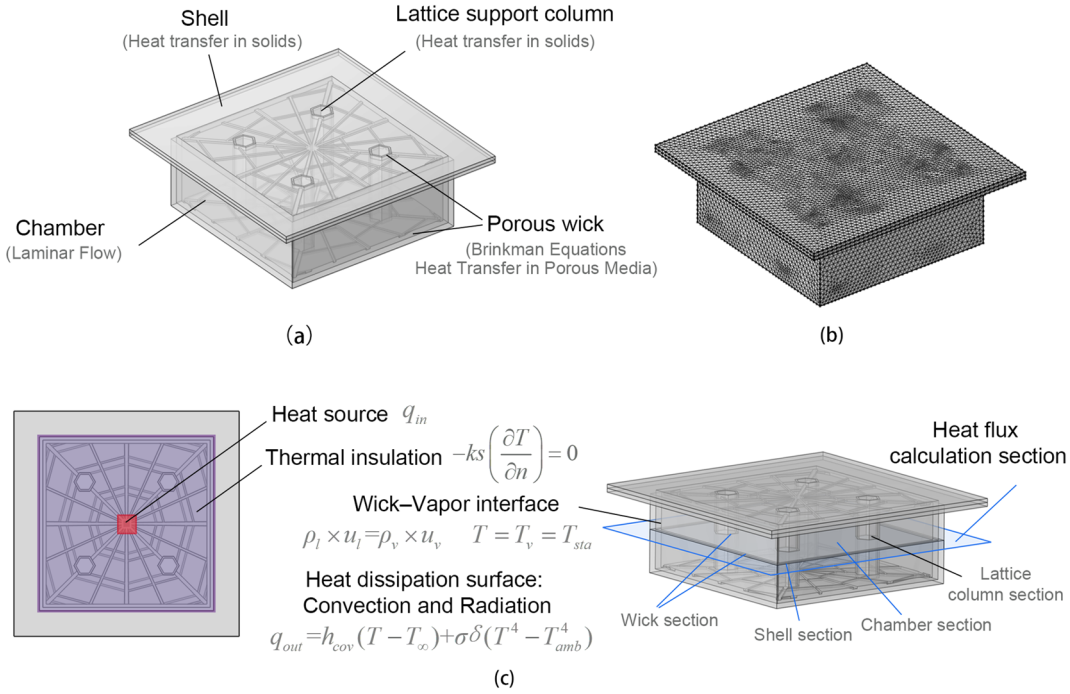


Figure 5. (**a**) Geometric model and its physical interface. (**b**) Diagram of the simulation model grid. (**c**) Boundary conditions and cross section for calculating heat transfer rate.

Table 5. Parameters in the finite element model.

Model Parameter	Value
Heat input, q_{in}	20 W
Convective heat transfer coefficient, h_{conv}	10 W/(m^2·K)
Emissivity, δ	0.95
Ambient temperature, T_{amb}	25 °C

For the surface of the shell, which is in contact with the heat source, a constant heat flux is applied as follows:

$$-k_s\left(\frac{\partial T_s}{\partial n}\right) = q_{in} \tag{11}$$

For the thermally insulated surface of the VC it is as follows:

$$-k_s\left(\frac{\partial T_s}{\partial n}\right) = 0 \tag{12}$$

For the heat dissipation surfaces, convection and radiation boundary conditions are applied as follows:

$$-k_s\left(\frac{\partial T_s}{\partial n}\right) = \underbrace{h_{conv}(T - T_\infty)}_{q_{conv}} + \underbrace{\sigma\delta\left(T^4 - T_{amb}^4\right)}_{q_{rad}} \tag{13}$$

where h_{conv} is the convective heat transfer coefficient, T_∞ is the temperature of surrounding fluid, is the σ is Stefan–Boltzmann constant, δ is the emissivity, and T_{amb} is the ambient temperature.

For the boundary condition at the wick–vapor interface, the mass and energy balance are as follows:

$$\begin{aligned} \rho_l u_l &= \rho_v u_v \\ T &= T_v = T_{sat} \end{aligned} \tag{14}$$

where T_v and T_{sat} are the vapor temperature and saturated wick temperature, respectively.

For the interface between vapor and the solid components (shell and lattice support columns), the boundary condition is as follows:

$$k_v\left(\frac{\partial T_v}{\partial n}\right) = k_s\left(\frac{\partial T_s}{\partial n}\right) \tag{15}$$

For the interface between wick and the solid components (shell and lattice support columns), the boundary condition is as follows:

$$k_{eff}\left(\frac{\partial T_w}{\partial n}\right) = k_s\left(\frac{\partial T_s}{\partial n}\right) \tag{16}$$

where k_{eff} is the effective thermal conductivity of the wick.

Table 6 shows the physical property parameters of the solid materials. The properties of the liquid working fluid material in the wicks adopt a liquid-phase system based on the IAPWS model (International Association for the Properties of Water and Steam Model). The gaseous material in the chamber adopts the ideal gas law for the vapor system.

Table 6. Physical properties of the materials.

Material	Density (kg/m^3)	Specific Heat Capacity (J/kg·K)	Thermal Conductivity W/(m·K)
Copper	8960	385	400
304 Stainless steel	7867	467	14.6

2.4.2. Grid Independence

To ensure the accuracy of the simulation results, this study assessed the impact of grid refinement on temperature. Stability is achieved with approximately 2.26×10^6 grids, and the temperature results obtained from the calculation tend to be stable, with the change in results from further grid refinement being less than 2%. As the further refinement of the grid increases the calculation cost, this study adopts a model with a grid range of 2.26×10^6 for finite element simulation.

3. Results and Discussion

3.1. Surface Modification Treatment of Evaporator and Condenser Wicks

Figure 6 shows the pretreated copper foam. When the deionized water drops on its surface, the liquid drop does not immediately penetrate the copper foam due to the solid–liquid contact angle between the droplet and the copper foam. After approximately 50 s, most of the liquid infiltrates the copper foam, with a thin liquid film remaining on the surface. In addition, as shown in the SEM image (Figure 6a), the pores of the copper foam, which are mainly interconnected, have different sizes and shapes, and have an open three-dimensional mesh structure.

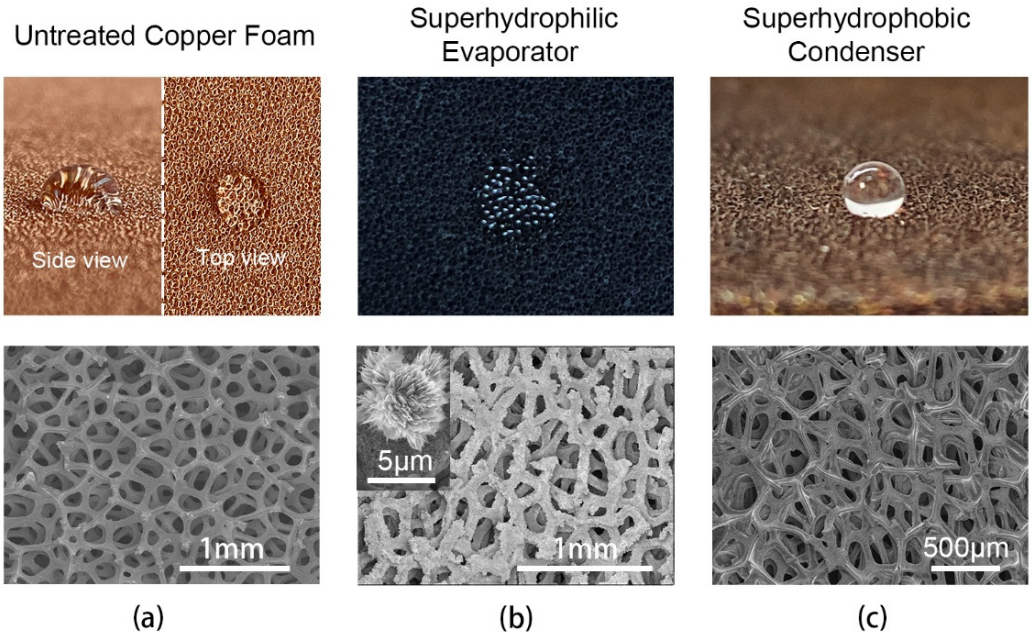


Figure 6. Wettability phenomenon and SEM images of deionized water on different copper foam surfaces: (**a**) untreated copper foam, (**b**) copper foam used for the evaporator wick, and (**c**) copper foam used for the condenser wick.

The superhydrophobic modified copper foam has a relatively low surface energy, and the contact angle of deionized water on its surface is relatively large. When the surface is slightly inclined, the liquid drop rolls, which is consistent with the rolling phenomenon of water drops on lotus leaves. Its SEM image is similar to that of the untreated sample, with no obvious microstructure or other phenomena. In addition, energy dispersive X-ray spectroscopy (EDS) in Figure 7a reveals that its main components are Cu, F, Si, and C.

When deionized water was dropped on the surface of the copper foam, which was treated via the superhydrophilic method, the liquid drop spread rapidly on the surface. Owing to its porosity, the copper foam is quickly penetrated by the liquid drop. Even in the unabsorbed stage, the contact angle between the liquid and the surface is extremely small.

The SEM image (Figure 6b) shows that the surface formed a nanoflower microstructure, and the EDS (Figure 7b) analysis shows that the nanoflower comprises Cu and O.

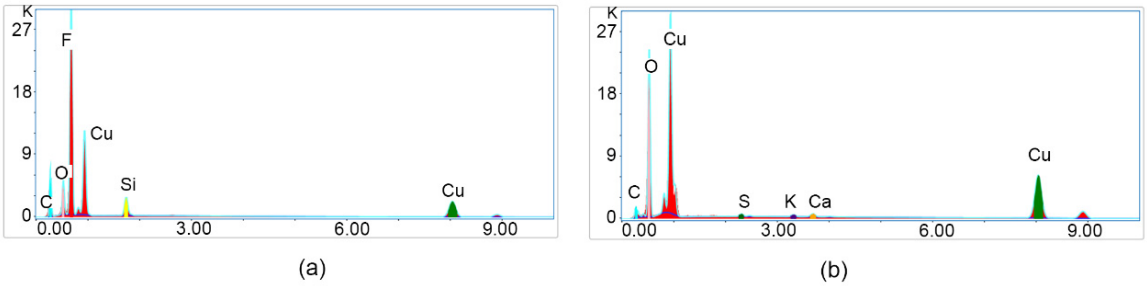


Figure 7. EDS element distribution in modified surface: (**a**) superhydrophobic and (**b**) superhydrophilic wicks.

Unlike the smooth surface of the untreated copper foam, the copper foam is full of nanoflower microstructures after superhydrophilic modification which increases the contact area and capillarity between the liquid and copper foam. According to the EDS analysis results, CuO was generated after the reaction. The hydroxyl group (-OH) on the surface of copper oxide can form strongly noncovalent and strongly hydrophilic hydrogen bonds with water molecules. Additionally, copper oxide has a high surface energy and a polar surface, which can exhibit strong superhydrophilic properties. According to the Young–Laplace equation, the contact angle of the liquid on the superhydrophilic wick is relatively small, thus providing a greater capillary force.

The superhydrophobic modified copper foam has a relatively low surface energy, and the contact angle of deionized water on its surface is relatively large. The adhesion between the liquid and the copper foam surface is too low for the liquid to spread. The reason is that perfluorodecyltriethylhydrosilane is a fluorinated compound that can combine with the copper surface via covalent or other chemical bonds. This surface modification process forms a highly hydrophobic fluorinated layer, considerably reducing the surface energy of copper foam to exclude water molecules. Hence, water drops do not easily attach to its surface, resulting in boiling and falling.

3.2. Thermal Performance of the VC by Experiments

3.2.1. Startup Performance of the VC

This study experimentally measured the time that is required for VCs to reach the steady state (the temperature change at each measuring point is less than 0.5 °C [19]) to evaluate the startup performance [34,35] of a traditional VC and the biomimetic designed VC under different filling ratios. As Figure 8 shows, when the filling ratios of the VC with traditional wicks are 10%, 20%, and 30%, the startup times are 3552 s, 4149 s, and 4276 s, respectively. The biomimetic optimized design (evaporator and condenser wicks with leaf vein grooves were conducted separately using superhydrophilic and superhydrophobic methods) considerably shortens the time required for the VC to reach the steady state. When the filling ratios are 10%, 20%, and 30%, the startup times for the VC using biomimetic designed wicks are 3284 s, 3663 s, and 3928 s, respectively. Compared with the traditional design, the biomimetic design significantly shortens the startup time by 7.5%, 11.7%, and 8.1%, respectively, and thus demonstrates a better startup characteristic.

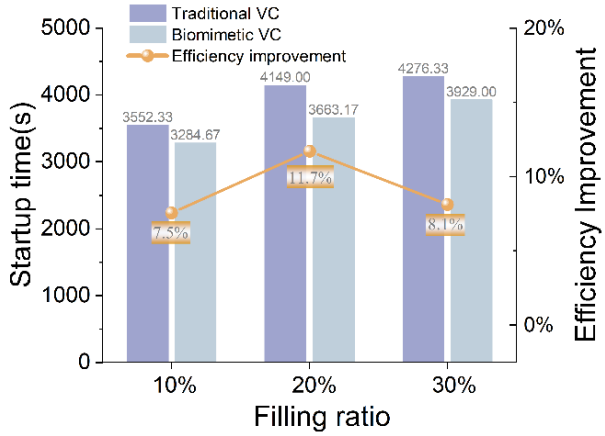


Figure 8. Comparison of steady-state time for traditional VC and biomimetic VC.

3.2.2. Isothermal Performance

As Figure 9 shows, compared with those of the biomimetic designed VC, the temperatures in the evaporation and condensation sections of the traditional VC are higher and lower, respectively. Specifically, for the three cases in which the liquid filling ratios are 10%, 20%, and 30%, under the same input temperature, the thermal uniformity performance of the VC is improved, with the temperature uniformity coefficient increasing from 75.36% to 79.64%, from 79.67% to 87.41%, and from 75.67% to 77.34%, respectively, in which the maximum increase is 7.74%, when the liquid filling ratio is 20%.

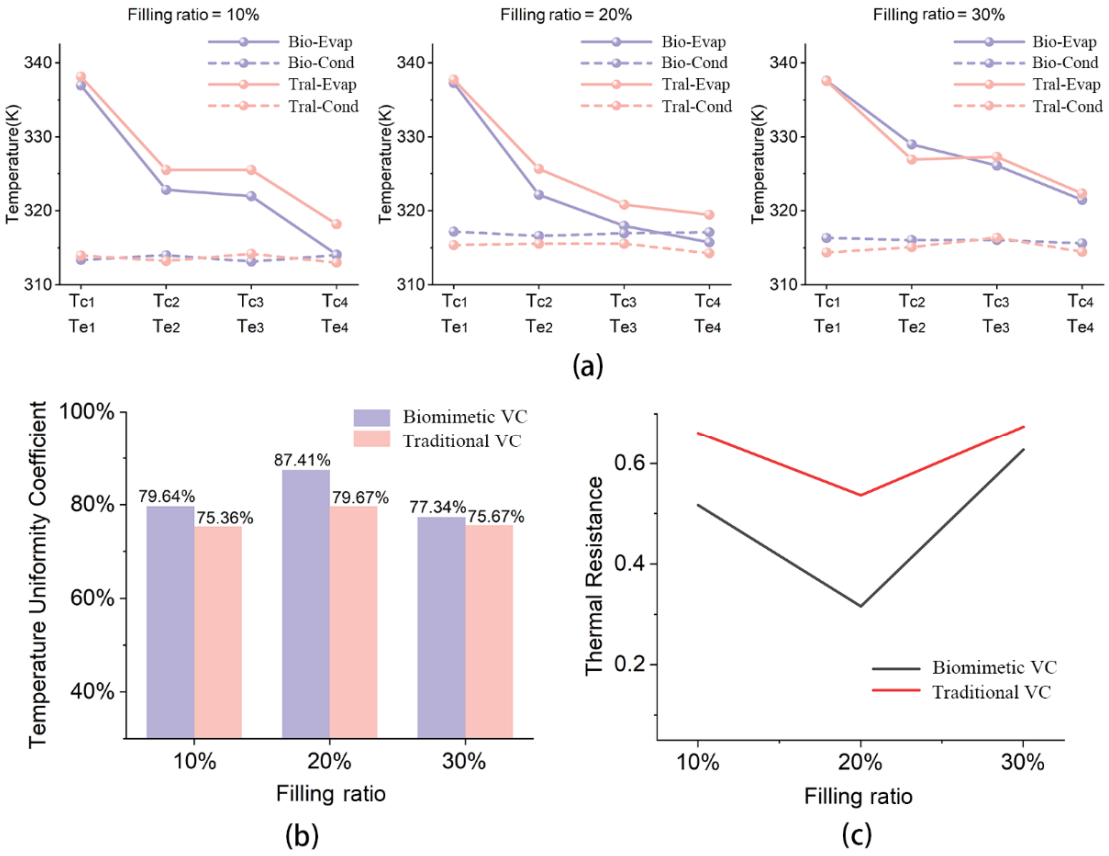


Figure 9. (**a**) Steady-state temperature of the VC. (**b**) Temperature uniformity coefficient of the VC. (**c**) Thermal resistance.

3.2.3. Thermal Resistance

As Figure 9c shows, the thermal resistance performance of the biomimetic vapor chamber is compared with that of the traditional vapor chamber under various liquid filling ratios. The thermal resistances of both VCs exhibit a non-monotonic relationship with increasing filling ratios, with them initially decreasing and then rising. The traditional VC achieves its minimum thermal resistance (approximately 0.54 °C/W) at the 20% filling ratio, while the biomimetic VC further reduces the thermal resistance to 0.32 °C/W under the same condition. In addition, the biomimetic VC demonstrates superior thermal performance across all filling ratios, particularly achieving a 40.74% reduction in thermal resistance compared to the traditional VC at 20% filling ratio.

When the filling ratio is 20%, both the traditional and biomimetic VC exhibit the minimum thermal resistance, suggesting that 20% may represent the optimal performance range for both structures [36]. Among all the three filling ratios investigated in this study, at the filling ratio of 10%, the insufficient working fluid fails to maintain a stable phase change for evaporation, leading to local drying and higher thermal resistance. At a filling ratio of 30%, the higher thermal resistance is due to excessive capillary flow resistance caused by the liquid and the reduction in the evaporation interface efficiency. In comparison, at a filling ratio of 20%, the liquid working fluid in the VC forms a continuous and stable capillary flow and efficiently vaporizes in the evaporation section, achieving a balance between capillary flow resistance and evaporation efficiency.

3.2.4. The Effect of Biomimetic Design on VC

The above results indicate that the biomimetic design has indeed enhanced the thermal performance of the vapor chamber. The superhydrophobic condensation section, inspired by the lotus leaf, enables the liquid working fluid to easily fall off, which can affect the vapor chamber in the following aspects. Firstly, it alters the condensation mode of the working fluid. In conventional condensation processes, the working fluid forms a continuous liquid film over the surface of the condenser wick, a phenomenon termed filmwise condensation. This regime inherently results in higher thermal resistance, as heat transfer to the cooling surface must occur through the insulating liquid film. In contrast, the superhydrophobic wick promotes dropwise condensation, where condensed droplets rapidly shed from the condensing section like water droplets on a lotus leaf. This transition significantly reduces liquid film resistance and enhances the effective contact area between the vaporized working fluid and the condenser surface. Secondly, it enhances the circulation of the liquid working fluid. The tiny droplets condensed on the superhydrophobic surface are guided by the biomimetic leaf vein grooves, which directs them toward the central region, where they then drip off. This facilitates the more efficient return of the working fluid to the heat source, enabling its participation in the subsequent phase change cycle. Consequently, the condensation efficiency and heat transfer performance are markedly improved.

The evaporation section, engineered with a moss-inspired superhydrophilic modification, allows liquid to infiltrate and spread more readily compared to traditional wicks, effectively mitigating local dry out phenomena. This enhances liquid transport efficiency and improves the operational stability of vapor chamber systems. On the other hand, compared to traditional copper foam wicks, CuO nanoflower structures on superhydrophilic surfaces provide a higher density of nucleation sites. This enhancement facilitates the initiation of boiling at a reduced degree of superheat and enhances the evaporation efficiency [37].

Overall, the biomimetic design optimizes liquid distribution and phase-change heat transfer, thereby enhancing the efficiency of evaporation–condensation cycles and reducing thermal resistance. In addition, we speculate that the enhancement of the heat transfer

performance is not only related to the biomimetic wicks but also to the composite lattice support columns. The wicks of the composite support columns add paths for the liquid working fluid to flow back to the evaporation section, which increases the instantaneous flow rate of the working fluid and further plays a role in temperature regulation.

3.3. Numerical Analysis of the VC

3.3.1. Thermal Performance of the VC by Numerical Analysis

In addition to experimental studies, the temperature distributions of the dry VC (with dry wicks, with no phase change) [38] and the phase-changing VC (with saturated wicks) in the steady state are also analyzed through numerical simulations. For the dry VC, the highest and lowest temperatures in the evaporation section are 444.15 K and 314.15 K, respectively, whereas those in the condensation section are 311.45 K and 307.85 K, respectively. The maximum temperature difference between the evaporation section and condensation section is 132 K. Thus, the VC without phase changes has a considerable temperature difference, which would be detrimental.

In contrast, the overall temperature difference in the VC with phase changes is relatively small. The highest and lowest temperatures in the evaporation section are 348.95 K and 318.05 K, respectively, and those in the condensation section are 318.35 K and 314.55 K, respectively. In this case, the temperature difference between the evaporation and condensation sections of the VC is considerably reduced. Although the evaporation section itself still has a certain temperature difference, it has greatly improved compared with that of the dry VC, and the phase-changing VC structure has achieved good uniformity.

A comparison of the simulation analysis results with the experimental results (Figure 10c) shows that the overall temperature of each measuring point in the dry VC is in good agreement, with an average error of 4.43%. When the phase-changing VC reaches a steady state, the simulation results of the surface temperature of the condensation section agree well with the experimental results, whereas those of the evaporation section are larger than the experimental results, and the discrepancy increases as the location approaches the heat source. This could be due to the simulation assuming an ideal state, while in the actual experimental measurements, temperature near the heat source is disturbed by the external environment, leading to larger temperature errors.

By integrating the cross sectional heat flux (W/m^2) of the shell, lattices, wicks, and chamber for the VC, the normal heat transfer rate (W) of the VC cross section can be calculated, and the contribution of each part of the VC structure to heat transfer can be analyzed. The comparison of the steady-state heat transfer rate in different sections of the two VC structures is shown in Table 7. For the dry VC, the heat transfer rates of the shell, lattices, wicks, and chamber are 2.3707 W, 0.65609 W, 4.2202 W, and 0.14581 W, respectively. For the phase-changing VC, the normal heat transfer rates of the shell, lattices, wicks, and vapor inside the chamber are 0.0012139 W, 6.2651×10^{-8} W, 4.6150×10^{-4} W, and -6.0641×10^{-5} W, respectively. The latent heat power of the working fluid in the chamber is 12.743 W, indicating that phase-changing heat transfer is the dominant mechanism for VC heat dissipation.

Table 7. Steady-state heat transfer rate in different sections of the vapor chamber.

Component	Dry VC (W)	Phase-Changing VC (W)
Shell	2.3707	0.0012139
Lattices	0.65609	6.2651×10^{-8}
Wicks	4.2202	4.6150×10^{-4}
Chamber	0.14581	6.0641×10^{-5}
Latent heat	0.0000	12.743

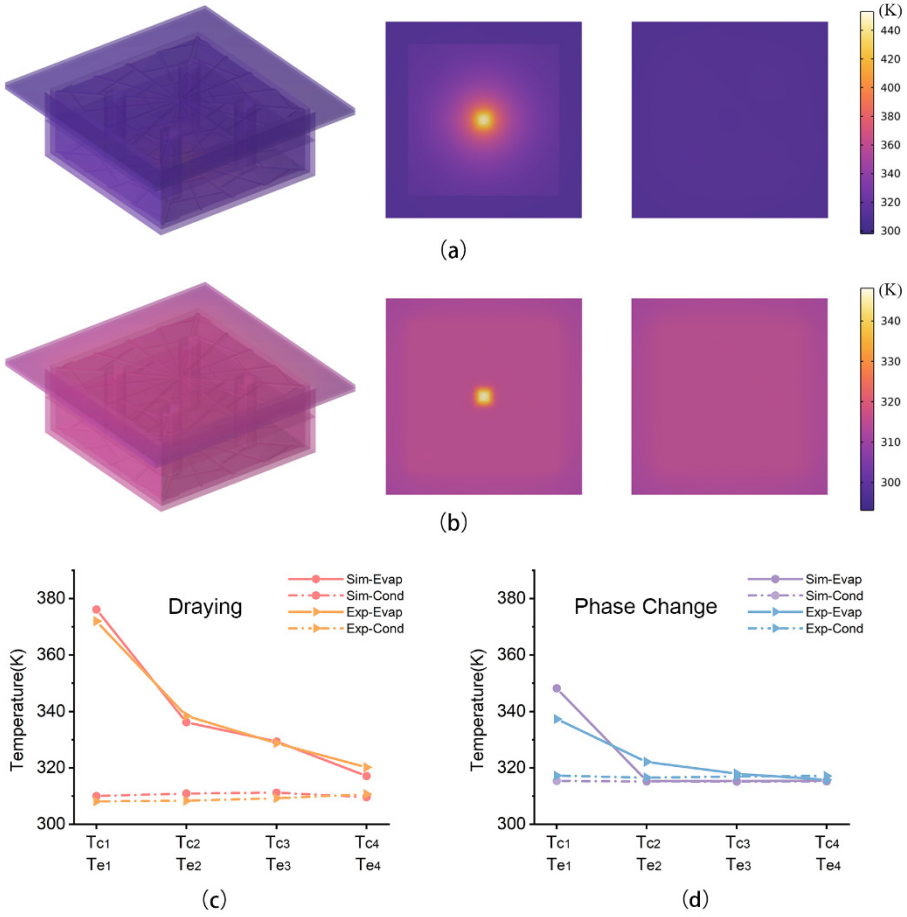


Figure 10. Temperature distribution diagram of the multiphysics simulation analysis results for the dry VC (**a**) and phase change VC (**b**); comparison of the simulation results and experimental results for the dry VC (**c**) and phase change VC (**d**).

The strong agreement between the simulation results of the numerical analysis and the experimental results indicates the efficiency of this simulation analysis method. A comparison of the temperature distributions of the VC in the dry state (without working fluid) and the phase-change steady state (Figure 10) clearly reveals that the VC based on phase change has better isothermal performance, which is attributed to the effect of the latent heat of the working fluid.

Furthermore, by comparing the heat transfer rate between each part of the dry VC and the phase change VC, the contribution of each part to heat transfer during the operation of the VC can be more accurately determined. For the dry VC, the stainless-steel shell and dry copper foam wicks provide the main contributions to heat transfer, whereas for the phase change VC, the latent heat transfer of the working medium is the dominant mechanism. For the same component, the heat transfer rate in the dry state is higher than that in the phase change state. According to Fourier's law, the larger the temperature difference is, the higher the heat transfer rate. The temperature difference between the evaporation and condensation sections in the VC without phase change is greater than that in the phase change state; therefore, there is a difference in the heat transfer rate.

In summary, the method for analyzing phase change structures on the basis of multiphysics simulation in this study can be used as an effective analytical method, especially for complex phase change systems. This method can be used to not only predict heat pipe performance but also provide a reference for structural optimization design.

3.3.2. Load-Bearing Mechanical Properties

Appropriate support structures not only improve the heat transfer of vapor chambers [23] but also play an important role in load-bearing performance. In this work, four composite support columns are uniformly set to improve the mechanical properties of the vapor chamber. Compared with that of the traditional structure without lattices, the weight of the VC with lattice supports is increased by 4.49%.

When the same force is applied in the vertical direction on the upper surface, the maximum strain is 0.088497 for the traditional VC shell and 0.045786 for the VC with the lattice support columns, and the latter is 48.26% lower than the former. The maximum stress changes from 25,764 MPa for the traditional structure to 16,562 MPa for the VC with lattice composite support columns, a 35.72% decrease.

The results show that when the same force is applied, the traditional structure is subjected to greater stress (Figure 11), whereas the structure with lattice support columns better distributes the load because of the lattice support, resulting in a smaller maximum stress and a more uniform stress distribution.

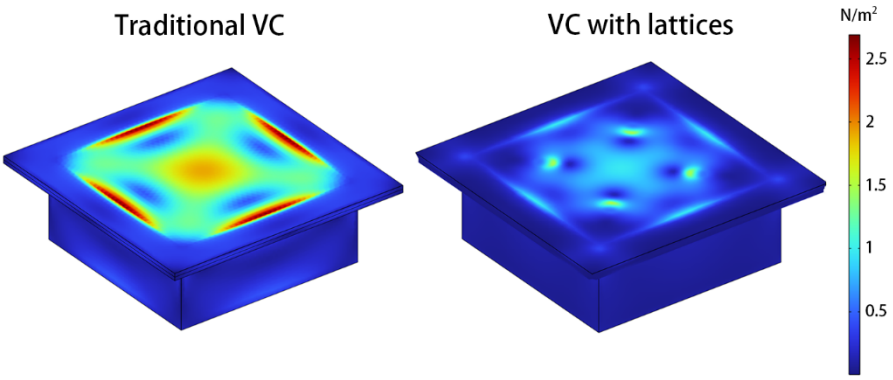


Figure 11. Stress distribution diagrams of traditional vapor chambers compared to vapor chambers with lattice support columns.

4. Conclusions

This study proposes a novel designed VC. Inspired by wettability phenomena and leaf vein capillary transport channels in nature, biomimetic wicks were designed, and the preparation of biomimetic composite wicks was realized through modification and precision milling processes. A honeycomb lattice support structure was designed and prepared via additive manufacturing technology, which was combined with a vertical wick to form a composite support column. This study investigated the thermal management performance of a VC through multiphysics numerical analysis and thermal performance experiments. The main conclusions are drawn as follows:

(1) Compared with the traditional VC, the novel VC has better startup characteristics and reaches the steady state sooner. When the filling ratios of the working fluid are 10%, 20%, and 30%, the startup time of the novel VC is shortened by 7.5%, 11.7%, and 8.1%, respectively. In particular, when the filling ratio is 20%, the biomimetic design increases the heat isothermal performance of the vapor chamber by up to 7.74%.

(2) The temperature distributions in the steady state of dry and phase-changing vapor chambers determined via multiphysics numerical analysis are consistent with the experimental measurement results, with average errors of 4.43% and 6.76%, respectively. This simulation method can predict the temperature and heat transfer rate of each part in the steady state, and thus is a great means to analyze, evaluate, and optimize the design of phase-changing devices.

(3) A composite support column based on a lightweight lattice improves the mechanical properties of the VC. When the same load is applied, the maximum strain of the shell is reduced by 48.26% compared with that of the traditional shell.

In summary, the comprehensive performance of the vapor chamber is enhanced by biomimetic optimized designs in this study, which provides a reference for phase-changing thermal management devices. However, existing research reveals that the chemical modification method adopted in this paper has certain drawbacks in terms of durability [39]. In the future, other modification technologies such as laser-based microstructure fabrication [40,41], plasma surface treatment [42], and chemical vapor deposition [43] can be considered to improve the stability and durability of the wick surface modification.

Author Contributions: J.S.: Conceptualization, Methodology, Validation, Investigation, Visualization, Writing—original draft preparation. C.G.: Supervision, Writing—review and editing, Funding acquisition. All authors have read and agreed to the published version of the manuscript.

Funding: Supported by the Research Fund of State Key Laboratory of Mechanics and Control for Aerospace Structures (Nanjing University of Aeronautics and astronautics) (Grant No. 1005-ZAG23011).

Data Availability Statement: Data underlying the results presented in this paper are available from the corresponding authors upon reasonable request.

Conflicts of Interest: The authors declare no conflict of interest.

References

1. Xu, H.; Yang, Y.; Gan, K.; Zhang, H.; Gao, Y.; Li, R.; Jiang, Y.; Qian, J.; Wei, Z.; Zheng, Y.; et al. Heat Transfer Performance of Novel High Temperature Flat Heat Pipe (HTFHP) with Heating Power and Inclination Angles. *Appl. Therm. Eng.* **2023**, *220*, 119679. [CrossRef]
2. Ma, Y.; Yu, H.; Huang, S.; Zhang, Y.; Liu, Y.; Wang, C.; Zhong, R.; Chai, X.; Zhu, C.; Wang, X. Effect of Inclination Angle on the Startup of a Frozen Sodium Heat Pipe. *Appl. Therm. Eng.* **2022**, *201*, 117625. [CrossRef]
3. Gou, J.; Liu, W. Feasibility Study on a Novel 3D Vapor Chamber Used for Li-Ion Battery Thermal Management System of Electric Vehicle. *Appl. Therm. Eng.* **2019**, *152*, 362–369. [CrossRef]
4. Luo, L.; Huang, B.; Bai, X.; Cheng, Z.; Jian, Q. Temperature Uniformity Improvement of a Proton Exchange Membrane Fuel Cell Stack with Ultra-Thin Vapor Chambers. *Appl. Energy* **2020**, *270*, 115192. [CrossRef]
5. Chen, G.; Tang, Y.; Duan, L.; Tang, H.; Zhong, G.; Wan, Z.; Zhang, S.; Fu, T. Thermal Performance Enhancement of Micro-Grooved Aluminum Flat Plate Heat Pipes Applied in Solar Collectors. *Renew. Energy* **2020**, *146*, 2234–2242. [CrossRef]
6. Xie, D.; Sun, Y.; Wang, G.; Chen, S.; Ding, G. Significant Factors Affecting Heat Transfer Performance of Vapor Chamber and Strategies to Promote It: A Critical Review. *Int. J. Heat Mass Transf.* **2021**, *175*, 121132. [CrossRef]
7. Ma, Y.; Wang, X.; Yu, H.; Huang, S.; Zhang, Y.; Su, G.H.; Deng, J.; Chai, X.; Hu, W. Capillary Limit of a Sodium Screen-Wick Heat Pipe. *Appl. Therm. Eng.* **2023**, *232*, 120972. [CrossRef]
8. Zhou, W.; Li, Y.; Huang, G.; Yang, Y.; Xu, L.; He, J.; Jian, Y. Thermal Performance of a Large-Diameter Thin Flattened Heat Pipe with Novel Composite Wick Structure. *Case Stud. Therm. Eng.* **2024**, *57*, 104352. [CrossRef]
9. Tang, H.; Weng, C.; Tang, Y.; Lu, Y.; Fu, T. Effect of Inclination Angle on the Thermal Performance of an Ultrathin Heat Pipe with Multi-Scale Wick Structure. *Int. Commun. Heat Mass Transf.* **2020**, *118*, 104908. [CrossRef]
10. Tang, H.; Tang, Y.; Wu, X.; Peng, R.; Sun, Y. Fabrication and Capillary Characterization of Multi-Scale Microgroove Wicks for Ultrathin Phase-Change Heat Transfer Devices. *Appl. Therm. Eng.* **2023**, *219*, 119621. [CrossRef]
11. Zhao, Z.; Li, L.; Wang, Y.; Wang, Y.; Hui, Y. Heat Transfer of Copper Mesh–Powder Composite-Based Sintered-Wick Vapor Chamber. *AIP Adv.* **2023**, *13*, 015027. [CrossRef]
12. Liu, T.; Yan, W.; Yang, X.; Wang, S. Improving the Thermal Performance of Thin Vapor Chamber by Optimizing Screen Mesh Wick Structure. *Therm. Sci. Eng. Prog.* **2022**, *36*, 101535. [CrossRef]
13. Sun, Q.; Zhi, G.; Zhou, S.; Dong, X.; Shen, Q.; Tao, R.; Qi, J. Advanced Design and Manufacturing Approaches for Structures with Enhanced Thermal Management Performance: A Review. *Adv Mater. Technol.* **2024**, *9*, 2400263. [CrossRef]
14. Li, Q.; Lan, Z.; Chun, J.; Lian, S.; Wen, R.; Ma, X. Fabrication and Capillary Characterization of Multi-Scale Micro-Grooved Wicks with Sintered Copper Powder. *Int. Commun. Heat Mass Transf.* **2021**, *121*, 105123. [CrossRef]

15. Ryu, S.; Lee, W.; Nam, Y. Heat Transfer and Capillary Performance of Dual-Height Superhydrophilic Micropost Wicks. *Int. J. Heat Mass Transf.* **2014**, *73*, 438–444. [CrossRef]
16. Peng, Y.; Liu, W.; Chen, W.; Wang, N. A Conceptual Structure for Heat Transfer Imitating the Transporting Principle of Plant Leaf. *Int. J. Heat Mass Transf.* **2014**, *71*, 79–90. [CrossRef]
17. Peng, Y.; Liu, W.; Wang, N.; Tian, Y.; Chen, X. A Novel Wick Structure of Vapor Chamber Based on the Fractal Architecture of Leaf Vein. *Int. J. Heat Mass Transf.* **2013**, *63*, 120–133. [CrossRef]
18. Li, B.; Yin, X.; Tang, W.; Zhang, J. Optimization Design of Grooved Evaporator Wick Structures in Vapor Chamber Heat Spreaders. *Appl. Therm. Eng.* **2020**, *166*, 114657. [CrossRef]
19. Cui, Z.; Jia, L.; Wang, Z.; Dang, C.; Yin, L. Thermal Performance of an Ultra-Thin Flat Heat Pipe with Striped Super-Hydrophilic Wick Structure. *Appl. Therm. Eng.* **2022**, *208*, 118249. [CrossRef]
20. Koukoravas, T.P.; Damoulakis, G.; Megaridis, C.M. Experimental Investigation of a Vapor Chamber Featuring Wettability-Patterned Surfaces. *Appl. Therm. Eng.* **2020**, *178*, 115522. [CrossRef]
21. Liu, C.; Hu, D.; Li, Q.; Chen, X.; Zhang, Z.; Zhou, F. Vapor Chamber with Two-Layer Liquid Supply Evaporator Wick for High-Heat-Flux Devices. *Appl. Therm. Eng.* **2021**, *190*, 116803. [CrossRef]
22. Liu, W.; Gou, J.; Luo, Y.; Zhang, M. The Experimental Investigation of a Vapor Chamber with Compound Columns under the Influence of Gravity. *Appl. Therm. Eng.* **2018**, *140*, 131–138. [CrossRef]
23. Li, D.; Huang, Z.; Zhao, J.; Jian, Q.; Chen, Y. Analysis of Heat Transfer Performance and Vapor–Liquid Meniscus Shape of Ultra-Thin Vapor Chamber with Supporting Columns. *Appl. Therm. Eng.* **2021**, *193*, 117001. [CrossRef]
24. Shen, J.; Guo, C.; Ma, Y.; Dong, A. Capillary Efficiency Study in Leaf Vein Morphology Inspired Channels. *Bioinspir. Biomim.* **2023**, *19*, 016006. [CrossRef]
25. Luo, Y.; Liu, W.; Huang, G. Fabrication and Experimental Investigation of the Bionic Vapor Chamber. *Appl. Therm. Eng.* **2020**, *168*, 114889. [CrossRef]
26. Feng, J.; Pang, Y.; Qin, Z.; Ma, R.; Yao, S. Why Condensate Drops Can Spontaneously Move Away on Some Superhydrophobic Surfaces but Not on Others. *ACS Appl. Mater. Interfaces* **2012**, *4*, 6618–6625. [CrossRef]
27. Ji, Y.; Chen, H.; Kim, Y.J.; Yu, Q.; Ma, X.; Ma, H.B. Hydrophobic Surface Effect on Heat Transfer Performance in an Oscillating Heat Pipe. *J. Heat Transf.* **2012**, *134*, 074502. [CrossRef]
28. Lu, L.; Xie, Y.; Zhang, F.; Liao, H.; Liu, X.; Tang, Y. Influence of a Sintered Central Column on the Thermal Hydraulic Performance of a Vapor Chamber: A Numerical Analysis. *Appl. Therm. Eng.* **2016**, *103*, 1176–1185. [CrossRef]
29. Li, D.; Huang, Z.; Liao, X.; Zu, S.; Jian, Q. Heat and Mass Transfer Characteristics of Ultra-Thin Flat Heat Pipe with Different Liquid Filling Rates. *Appl. Therm. Eng.* **2021**, *199*, 117588. [CrossRef]
30. Yang, Y.; Li, J.; Wang, H.; Liao, D.; Qiu, H. Microstructured Wettability Pattern for Enhancing Thermal Performance in an Ultrathin Vapor Chamber. *Case Stud. Therm. Eng.* **2021**, *25*, 100906. [CrossRef]
31. Gu, Z.; Yang, K.; Liu, H.; Zhou, X.; Xu, H.; Zhang, L. Enhancing Heat Transfer Performance of Aluminum-Based Vapor Chamber with a Novel Bionic Wick Structure Fabricated Using Additive Manufacturing. *Appl. Therm. Eng.* **2024**, *247*, 123076. [CrossRef]
32. Zhang, H.; Ye, F.; Guo, H.; Yan, X. Isothermal Performance of Heat Pipes: A Review. *Energies* **2022**, *15*, 1992. [CrossRef]
33. Huang, G.; Liu, W.; Luo, Y.; Li, Y. A Novel Ultra-Thin Vapor Chamber for Heat Dissipation in Ultra-Thin Portable Electronic Devices. *Appl. Therm. Eng.* **2020**, *167*, 114726. [CrossRef]
34. Dan, D.; Li, W.; Zhang, Y.; Xie, Y. A Quasi-Dynamic Model and Thermal Analysis for Vapor Chambers with Multiple Heat Sources Based on Thermal Resistance Network Model. *Case Stud. Therm. Eng.* **2022**, *35*, 102110. [CrossRef]
35. Ji, X.; Wang, Y.; Xu, J.; Huang, Y. Experimental Study of Heat Transfer and Start-up of Loop Heat Pipe with Multiscale Porous Wicks. *Appl. Therm. Eng.* **2017**, *117*, 782–798. [CrossRef]
36. Liu, Y.; Han, X.; Shen, C.; Yao, F.; Zhang, M. Experimental Study on the Evaporation and Condensation Heat Transfer Characteristics of a Vapor Chamber. *Energies* **2019**, *12*, 11. [CrossRef]
37. Yin, L.; Yang, Z.; Zhang, K.; Xue, Y.; Dang, C. Heat Transfer of Water Flow Boiling in Nanostructured Open Microchannels. *Energies* **2023**, *16*, 1303. [CrossRef]
38. Xia, Y.; Yao, F.; Wang, M. Experimental Investigation on Thermal Performance of Vapor Chambers with Diffident Wick Structures. *Energies* **2023**, *16*, 6464. [CrossRef]
39. Malla, L.K.; Dhanalakota, P.; Dileep, H.; Mahapatra, P.S.; Pattamatta, A. Surface Wettability Modifications and Applications in Wickless Heat Pipes. *Surf. Interfaces* **2024**, *45*, 103837. [CrossRef]
40. Guo, Y.; Zhao, H. Femtosecond Laser Processed Superhydrophobic Surface. *J. Manuf. Process.* **2024**, *109*, 250–287. [CrossRef]
41. Tong, W.; Xiong, D. Direct Laser Texturing Technique for Metal Surfaces to Achieve Superhydrophobicity. *Mater. Today Phys.* **2022**, *23*, 100651. [CrossRef]

42. Hovish, M.Q.; Hilt, F.; Rolston, N.; Xiao, Q.; Dauskardt, R.H. Open Air Plasma Deposition of Superhydrophilic Titania Coatings. *Adv. Funct. Mater.* **2019**, *29*, 1806421. [CrossRef]
43. Vilaró, I.; Yagüe, J.L.; Borrós, S. Superhydrophobic Copper Surfaces with Anticorrosion Properties Fabricated by Solventless CVD Methods. *ACS Appl. Mater. Interfaces* **2017**, *9*, 1057–1065. [CrossRef] [PubMed]

Disclaimer/Publisher's Note: The statements, opinions and data contained in all publications are solely those of the individual author(s) and contributor(s) and not of MDPI and/or the editor(s). MDPI and/or the editor(s) disclaim responsibility for any injury to people or property resulting from any ideas, methods, instructions or products referred to in the content.